PCCP

PAPER

View Article Online
View Journal | View Issue

Cite this: *Phys. Chem. Chem. Phys.*, 2018, **20**, 15960

Polymorphism and metal-induced structural transformation in 5,5′-bis(4-pyridyl)-(2,2′-bispyrimidine) adlayers on Au(111)†

Diana Hötger,[a] Pilar Carro,[b] Rico Gutzler,[a] Benjamin Wurster,[a] Rajadurai Chandrasekar,[c] Svetlana Klyatskaya,[c] Mario Ruben,[cd] Roberto C. Salvarezza,[e] Klaus Kern[af] and Doris Grumelli*[e]

Received 16th November 2017,
Accepted 26th April 2018

DOI: 10.1039/c7cp07746g

rsc.li/pccp

Metal–organic coordination networks self-assembled on surfaces have emerged as functional low-dimensional architectures with potential applications ranging from the fabrication of functional nanodevices to electrocatalysis. Among them, bis-pyridyl-bispyrimidine (PBP) and Fe-PBP on noble metal surfaces appear as interesting systems in revealing the details of the molecular self-assembly and the effect of metal incorporation on the organic network arrangement. Herein, we report a combined STM, XPS, and DFT study revealing polymorphism in bis-pyridyl-bispyrimidine adsorbed adlayers on the reconstructed Au(111) surface. The polymorphic structures are converted by the addition of Fe adatoms into one unique Fe-PBP surface structure. DFT calculations show that while all PBP phases exhibit a similar thermodynamic stability, metal incorporation selects the PBP structure that maximizes the number of metal–N close contacts. Charge transfer from the Fe adatoms to the Au substrate and N–Fe interactions stabilize the Fe-PBP adlayer. The increased thermodynamic stability of the metal-stabilized structure leads to its sole expression on the surface.

Introduction

Two-dimensional metal–organic coordination networks (2D-MOCNs) self-assembled on surfaces under well-controlled conditions constitute a promising route to fabricate functional nanodevices and new (electro)catalysts.[1–3] 2D-MOCNs can be synthesized using organic precursors that interact on a metal substrate with small doses of evaporated metal atoms such as transition and lanthanide metals under ultra-high vacuum (UHV) conditions.[4–6] In some cases, the MOCN is formed by first adsorbing a monolayer of the metal-free ligand on a metal single-crystal surface such as Cu(100),[7] Ag(111),[8] and Au(111).[9] Subsequently, a stoichiometric amount of a metal is vapor deposited. It is likewise possible to deposit first metal clusters on the substrate followed by the organic molecules that induce cluster dissolution and MOCN formation.[10–12] The metal atoms are readily coordinated by the ligand molecules and adopt different oxidation states, for example Fe(II) when coordinated to four carboxylates,[13] Co(0) when coordinated to nitriles,[11] Pt(II) and V(II)/V(III) within a nitrogen coordination environment,[14,15] or Cu(0) coordinated to pyridyl groups.[16] In this way, monolayers of different 2D-MOCNs with a high degree of metalation have been produced. Additionally, the complexity of the metal–organic network could increase as metal adatoms from the substrate seem to interact with the organic adlayer.[17–19] These experiments have revealed the interplay between molecule–adatom, intermolecular, and adsorbate–substrate interactions that result in 2D-MOCN formation.[3] The main features of these structures on metal substrates are the metal center–molecule and metal center–substrate interactions since they determine the physical and chemical properties of the 2D-MOCN systems. The latter varies strongly with the type of the incorporated metal center. This can be observed exemplarily for Fe, Co, and Ni ions in porphyrins, which interact differently with supporting substrates. Photoelectron spectroscopy reveals the formation of strong bonds between Co/Fe and Ag(111)[20,21] although on Au(111) the situation is complicated by the herringbone reconstruction.[22] In contrast,

[a] *Max Planck Institute for Solid State Research, Heisenbergstrasse 1, D-70569 Stuttgart, Germany*
[b] *Área de Química Física, Departamento de Química, Facultad de Ciencias, Universidad de La Laguna, Instituto de Materiales y Nanotecnología, Avda. Francisco Sánchez, s/n 38200-La Laguna, Tenerife, Spain*
[c] *Institute of Nanotechnology (INT), Karlsruhe Institute of Technology (KIT), 76344 Eggenstein-Leopoldshafen, Germany*
[d] *IPCMS-CNRS, Université de Strasbourg, 23 rue de Loess, 67034, Strasbourg, France*
[e] *Instituto de Investigaciones Fisicoquímicas Teóricas y Aplicadas (INIFTA), Facultad de Ciencias Exactas, Universidad Nacional de La Plata – CONICET – Sucursal 4 Casilla de Correo 16, (1900) La Plata, Argentina. E-mail: doris@inifta.unlp.edu.ar*
[f] *Institut de Physique, École polytechnique fédérale de Lausanne, 1015 Lausanne, Switzerland*

† Electronic supplementary information (ESI) available. See DOI: 10.1039/c7cp07746g

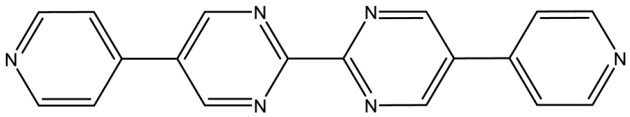

Scheme 1 5,5′-Bis(4-pyridyl)(2,2′-bipyrimidine) (PBP).

Ni ions are much less influenced by Ag(111).[23] On the other hand, the metal–organic molecule interactions determine the coordination number and also induce structural transformations.[24]

In this work, we study the organization of bis-pyridyl-bispyrimidine (PBP) molecules (Scheme 1) on the reconstructed Au(111) surface before and after the addition of Fe adatoms by using scanning tunneling microscopy (STM), X-ray photoelectron spectroscopy (XPS) and first principles density functional theory (DFT) calculations including van der Waals (vdW) interactions. The PBP ligand was synthesized according to an earlier established protocol.[25] The PBP molecules spontaneously adsorb by the sublimation of PBP on Au(111) to form a monolayer that rearranges into a stable Fe–N coordinated system after Fe deposition.[26] Our results reveal that the PBP molecules organize in different surface structures on the unperturbed herringbone reconstruction. These structures have similar thermodynamic stability; however, in contact with Fe adatoms only one of these PBP structures survives indicating that Fe adatom/organic molecule/substrate interactions rearrange the different surface structures into one stable phase. DFT analysis of the different models indicates that charge transfer from the Fe adatoms to the Au substrate and N–Fe interactions stabilize the Fe-PBP adlayer, which is evidenced in Fe and N core-level spectra. The increase in the Fe–N coordination is the driving force for the prevalence of one single structure. This study provides a detailed understanding of the role of metal adatom/organic molecule/substrate interactions in the reorganization and stability of 2D-MOCNs on well-defined single crystal faces, a key piece of knowledge for controlled fabrication of functional low-dimensional structures.

Results and discussion

STM images of the reconstructed Au(111) surface after PBP adsorption are shown in Fig. 1. Different surface structures (phases: I, linear; II, grid; III, zig-zag) coexist on the substrate terraces, which still exhibit the typical pattern of the $22 \times \sqrt{3}$ (herringbone) reconstruction on either the covered or small uncovered PBP regions.

In general, the herringbone reconstruction is lifted upon strong molecular adsorption, thus, the STM images in Fig. 1 suggest a weak PBP–Au(111) interaction. However, it has been recently shown that N-heterocyclic carbenes,[27] perylene-3,4,9,10-tetracarboxylic acid bisimides,[28] and isocyanide[28] strongly adsorb on the reconstructed Au(111) surface in UHV without lifting the herringbone reconstruction, leading to the formation of gold–organic hybrids formed by covalently bonded molecule–Au adatom complexes.[29] Furthermore, Au adatoms were also coordinated to weakly adsorbed porphyrins on the Au(111) surface, which has been shown by STM.[17] Therefore we have explored the possible

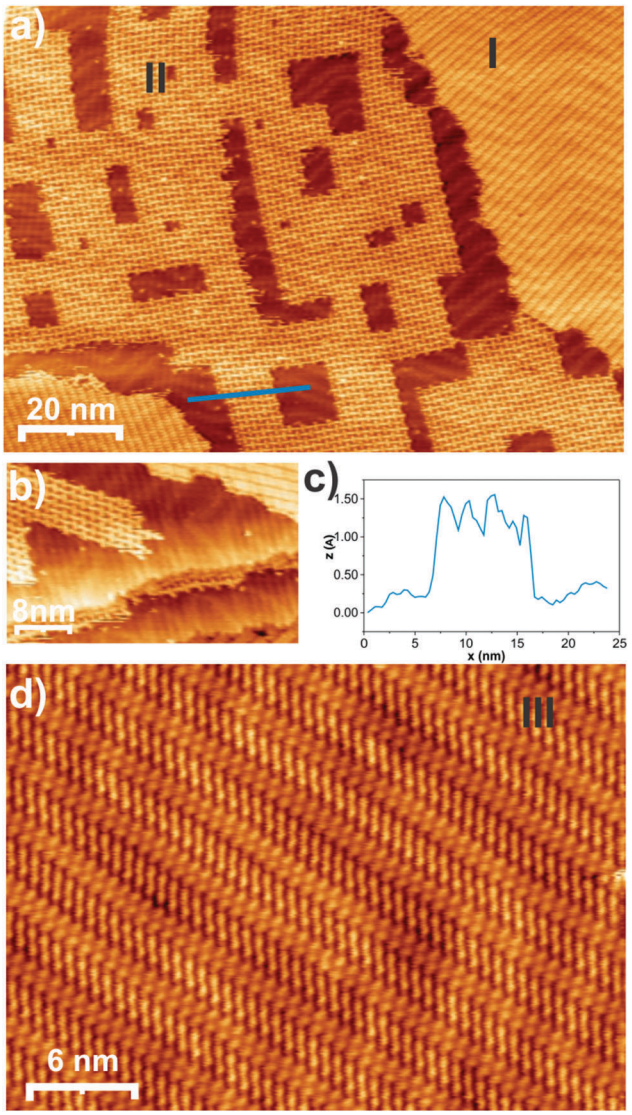

Fig. 1 UHV STM images. (a) Large-scale image of phases I and II and (b) zoom showing the details of the domains and step edges of phases I and II. (c) Cross-section analysis between covered and uncovered (clean Au) PBP regions (blue solid line) in (a). (d) Large-scale image of phase III.

presence of Au adatoms underneath the different PBP domains by analyzing the relative height difference (Δh) between small Au regions not covered by molecules and the PBP-covered domains (Fig. 1c). The cross-section analysis results in $\Delta h \approx 1.2$–1.6 Å. In principle, this difference suggests that the molecular domains do not contain significant amounts of Au adatoms underneath the molecules, as in this case one expects $\Delta h = 2.4$ Å.[27] Therefore, the bright spots shown in Fig. 1 are mainly assigned to PBP molecules although we cannot completely discard that small amounts of Au adatoms coming from step edges can be incorporated into some domains between the molecules as will be discussed later on the basis of DFT calculations. This is particularly true considering that STM images are a convolution of topographic and electronic effects. In addition, we studied deposition time (Table SI-1, ESI†) and post-annealing temperature dependence (Fig. SI.2, ESI†) of the coverage of the different molecular phases before Fe incorporation. The STM

images reveal that the most stable phase at both short deposition times and low post-annealing temperatures is, indeed, phase II. In fact, only by increasing deposition time or annealing temperature the coverage of the linear and zig-zag phases becomes important. The initial higher stability for the grid phase compared with linear and zig-zag phases in the absence of Fe might suggest that available Au adatoms could provide an extra stabilization of phase II during its formation. Once there are no more available Au adatoms, the other two phases start to appear and compete with phase II.

Fig. 1a and b also contains interesting information about how these phases are formed. The border of the grid-shaped domains consists of PBP molecules in an open structure[12] where most of the molecules remain aligned to the reconstruction lines as can be seen in Fig. 1b. On the other hand, the linear phase is formed by the molecules with their long axis aligned almost perpendicular or parallel to the reconstruction lines with disordered molecules at the growing domain boundaries (Fig. 1a). Also, the molecules in the zig-zag domains follow the domain walls of the herringbone reconstruction (Fig. 1d). It is evident that the substrate acts as a template for the different phases, which is also reflected in the rotation of domains by 120° with respect to each other (see the example in Fig. SI.1, ESI†). Finally, the molecular domains are preferentially nucleated at the lower part of the step edges and grow from these sites to the adjacent terraces.

The high-resolution images of the different phases show that they are formed by individual PBP molecules that appear as dumbbell-shaped objects (Fig. 2a–c). From the molecular dimensions, we assign each lobe to one of the pyridyl–pyrimidine parts of the PBP molecule. Phase I consists of a nearly linear array of molecules (Fig. 2a), which has been previously reported on Au(111).[26,30] Phase II exhibits the molecules organized in grid-shaped patterns (Fig. 2b), which has not been yet reported for Fe-free PBP molecules, *i.e.* they have been only observed after Fe incorporation into the PBP network.[26] Two unit cells are drawn: the more simple-centered square cell (Fig. 2b light grey), and for consistency the oblique cell (Fig. 2b dark grey) used in previous studies.[25,26] Finally, phase III consists of the molecules organized in zig-zag patterns (Fig. 2c), which has been already described for the molecule on Ag(111)[25] but not for Au(111).

Taking into account the STM images and unit cell dimensions for these phases, the surface coverage θ is, in all cases, slightly smaller than $\theta = 0.05$ (Table 1). The linear and zig-zag patterns result from pyridyl–pyridyl (long molecular axis) and pyrimidine–pyrimidine (short molecular axis) organization while the grid-shaped patterns involve the pyridyl–pyrimidine arrangement. Note that in all cases the N···H distance is $\approx$6 Å, a value too large to expect stabilization *via* hydrogen bonding.

Interestingly, after Fe vaporization phase II dominates the substrate surface (Fig. 3a and b), indicating that a metal–organic reaction induces almost complete rearrangement of phases I and III into phase II. While the adsorbed Fe species are not observed in the STM images, as it was reported for adsorbed Co in MOCNs,[11] their presence is clearly revealed by the changes in the N 1s and Fe 2p XPS of the samples (Fig. 3c and d). The N 1s signal of the PBP sample without Fe shows one peak which can be decomposed into two contributions, one from N in the bipyrimidine part of PBP and one from nitrogen in the pyridyl groups (Fig. 3c). The peak centered at 399.1 eV is fitted with a Voigt function of twice the area as the peak centered at 398.5 eV. This ratio represents the stoichiometry of N = 4 in the bipyrimidine part and 2 in the pyridyl groups per molecule. This assignment of the higher binding energy peak to the bipyrimidine nitrogen and the lower binding energy peak to the pyridyl nitrogen is supported by the literature.[31,32] A broad peak at a high binding energy (red) was added during fitting to account for the asymmetric shape of the N 1s signal whose origin is not clear. Possible origins for the asymmetric tail are the use of the non-monochromatic X-ray light source, shake-up satellites from intramolecular excitations, or from hydrogen-bonded molecules in what might be small patches of multilayers on the surface.[33] We note that the need to fit a broad high-energy peak can be removed by fitting asymmetric line shapes instead of the Voigt functions, while leaving the positions of the maxima of the fit functions unchanged. Upon the addition of Fe to the PBP network, the N 1s peak shifts towards a higher binding energy and broadens considerably. The asymmetric line shape can again be deconvoluted by two Voigt functions with an area ratio of 2 : 1. The addition of a broad peak at the high binding energy improves the fit quality slightly but has only negligible effect on the position of the two main peaks. The low binding energy peak is located at 398.9 eV, and the high binding energy peak is located at 399.9 eV. The contribution assigned to the bipyrimidine N is shifted towards a higher binding energy by 0.8 eV while the pyridine nitrogen

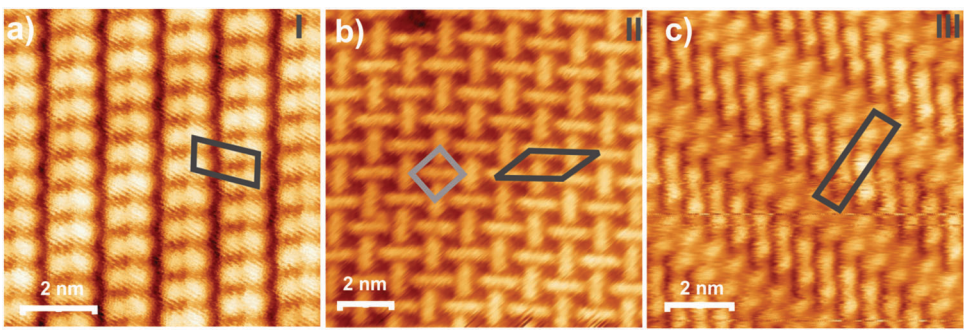

Fig. 2 UHV STM images. (a) Phase I, linear; (b) phase II, grid; (c) phase III, zig-zag. Unit cells are indicated in dark grey. For phase II: centered square cell in light grey is also highlighted.

Table 1 Experimental and theoretical parameters and energetic and structural data for PBP and Fe-PBP surface structures

Surface structure	Without Fe			With Fe		
Phase	PBP I Linear	PBP III zig-zag	PBP II grid	Au-PBP II grid	Fe-PBP	Fe-PBP strained Au
Unit cell	$\begin{pmatrix} 3 & 0 \\ 5 & 7 \end{pmatrix}$	$\begin{pmatrix} 3 & 0 \\ 14 & 7 \end{pmatrix}$	$\begin{pmatrix} 9 & 0 \\ -2 & 5 \end{pmatrix}$	$\begin{pmatrix} 9 & 0 \\ -2 & 5 \end{pmatrix}$	$\begin{pmatrix} 9 & 0 \\ -2 & 5 \end{pmatrix}$	$\begin{pmatrix} 9 & 0 \\ -2 & 5 \end{pmatrix}$
θ_{PBP}	0.048	0.048	0.044	0.044	0.044	0.044
θ_{Fe}	—	—	—	—	0.088	0.088
E_{ads}/eV	−2.39	−4.76	−4.24	−3.64	−24.68	−26.54
γ/meV Å^{-2}	−15.19	−15.10	−12.60	−21.59	−73.22	−86.04
Theoretical unit cell parameters	a = 18.47 Å b = 8.82 Å α = 76.1°	a = 35.66 Å b = 8.82 Å α = 90°	a = 25.48 Å b = 18.37 Å α = 46.1°	a = 25.48 Å b = 18.37 Å α = 46.1°	a = 25.48 Å b = 18.37 Å α = 46.1°	a = 24.4 Å b = 17 Å α = 46.1°
Experimental unit cell parameters	a = 17.3 Å ± 1.8 b = 9.2 Å ± 0.5 α = 77° ± 2	a = 33.6 Å ± 3.5 b = 8.1 Å ± 0.8 α = 92° ± 4	a = 24.5 Å ± 1.5 b = 16.8 Å ± 1.8 α = 44° ± 2	a = 24.5 Å ± 1.5 b = 16.8 Å ± 1.8 α = 44° ± 2	a = 24.5 Å ± 1.5 b = 16.8 Å ± 1.8 α = 44° ± 2	

peak is shifted by 0.4 eV. This shift towards the higher binding energy upon metal coordination to nitrogen is reminiscent of a peak shift of 0.5 eV of the iminic nitrogen in free-base porphyrins upon metalation with iron,[20] and is supported theoretically for nitrogen in a carbon matrix.[34] The Fe cation presumably stabilizes the N 1s core-level electrons through electrostatic interactions and thus raises its binding energy. Note that, in this case, a third component at a higher BE is not needed for a good fitting of the experimental peak, suggesting that the origin of this component is hydrogen bonding in some PBP multilayer patches that have been removed during the heating of the PBP layer.

The Fe 2p signal of Fe-PBP is rather broad with $2p_{3/2}$ and $2p_{1/2}$ peaks (Fig. 3d) and shows a smooth but non-linear background on the clean Au(111) surface (gray), which hinders the removal of acceptable background. Although a deconvolution with fit functions is hence not possible, we can still qualitatively analyze the $2p_{3/2}$ peak. The main feature of the $2p_{3/2}$ peak is centered around 710 eV, roughly corresponding to Fe in its oxidized form Fe(II). A small shoulder at a lower binding energy of about 707 eV originates possibly from metallic iron. The origin of the broad structure at a higher binding energy is presumably due to the multiplet structure and has been suggested to stem from shake-up processes from electronic excitations in the organic ligand.[35] The oxidized form of Fe that is observed in XPS could be explained by charge transfer from the Fe adatoms to the Au substrate while the shift in the N 1s spectrum could be produced by the coordination of Fe to the N atoms.[36] The excess Fe that is not coordinated to molecules can form clusters (see the arrows in Fig. 3a) on the surface and leads to the Fe(0) signal in the Fe 2p spectrum, although interactions with special sites of the Au(111) surface of coordinated Fe can also lead to Fe(0).[35]

Note that both coordinated Au and Fe atoms into the grid structure in phase II cannot be observed by STM, but Fe coordination has been revealed by XPS. Likely, the Au atoms will be replaced by the more reactive Fe species, a fact that will be clarified by our DFT calculations.

DFT calculations were done in order to model the different surface structures with and without addition of Fe. Before we discuss these results, it should be noted that the dimensions of the unit cells used to represent the adsorbate overlayers of this study do not match the $(22 \times \sqrt{3})$ unit cell needed to consider the Au herringbone reconstruction, thus we are forced to use the Au(111)-(1×1) unreconstructed unit cell. We will include this simplification later in our discussion.

Fig. 4a–c shows all the optimized structures for the PBP lattices observed on the Au surface. Phases I and III correspond to $\begin{pmatrix} 3 & 0 \\ 5 & 7 \end{pmatrix}$ (Fig. 4a) and $\begin{pmatrix} 3 & 0 \\ 14 & 7 \end{pmatrix}$ (Fig. 4b) lattices with unit cell dimensions that fairly agree with those determined by the STM images (Table 1). The molecular density of these surface structures is 6.4×10^{-3} Å^{-2}, and, therefore, its surface coverage is θ = 0.048 (Table 1). In both cases, the molecules adopt a planar configuration with a PBP–Au(111) distance of 3.2 Å implying physisorption of the molecules on the substrate. The adsorption energies are E_{ads} = −2.39 eV for phase I (only one PBP per unit cell) and E_{ads} = −4.76 eV for phase III (two PBP per unit cell) (Table 1), mainly resulting from π-electron interactions between the aromatic rings of the molecules and the Au(111) surface. The physisorbed state is reflected in the small surface free energies of these lattices γ = −15.19 meV Å^{-2} and γ = −15.10 meV Å^{-2}. On the other hand, phase II (Fig. 4c) corresponds to a $\begin{pmatrix} 9 & 0 \\ -2 & 5 \end{pmatrix}$ unit cell with a unit cell dimension that is also consistent with that experimentally observed in the STM images (Table 1). Also in this case, the molecules are physisorbed on the surface adopting a planar configuration with a vertical distance PBP-Au(111) of 3.3 Å. Therefore, the experimental molecule–substrate height difference of 1.2/1.6 Å (Fig. 1c) results from a convolution of topographic and electronic effects. Phases I–III are predominantly stabilized by substrate–molecule interactions, resulting in dense packing with little van der Waals intermolecular interaction. Analyzing the energetics for phase II, the molecular density and surface coverage are slightly smaller (5.9×10^{-3} Å^{-2} and θ = 0.044) than those observed for phases I and III. As expected for the lower surface coverage, the stability is also slightly lower than that found for phases I and III, γ = −12.60 meV Å^{-2} (Table 1). However, when Au atoms are incorporated into this phase, most of them adopt a Au–N3 configuration and those in the [1$\bar{1}$0] direction adopt a Au–N2 coordination, and the surface free energy amounts to γ = −21.59 meV Å^{-2}, *i.e.* this lattice becomes more stable than phases I and III. This may explain why phase II is the initial

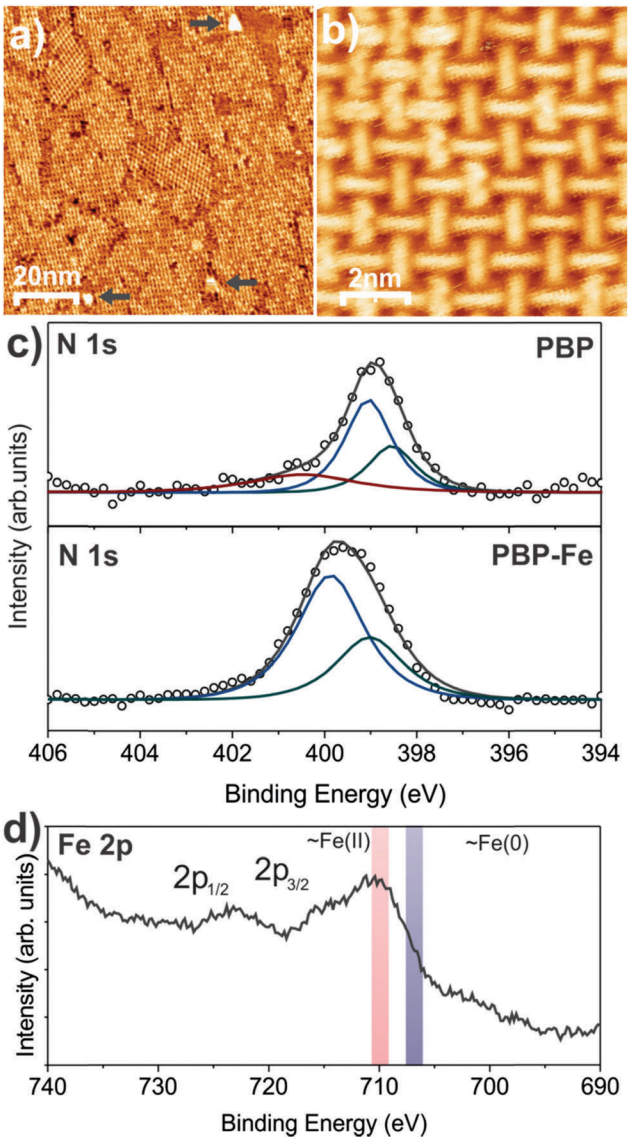

Fig. 3 UHV STM images after Fe incorporation into the PBP network. (a) Overview of the STM topograph and (b) zoomed-in STM topograph. (c) XPS N 1s before (upper panel) and after Fe incorporation (lower panel). The two fit functions correspond to nitrogen in bipyrimidine (larger peak) and pyridyl (smaller peak) and (d) XPS Fe 2p of Fe-PBP/Au(111).

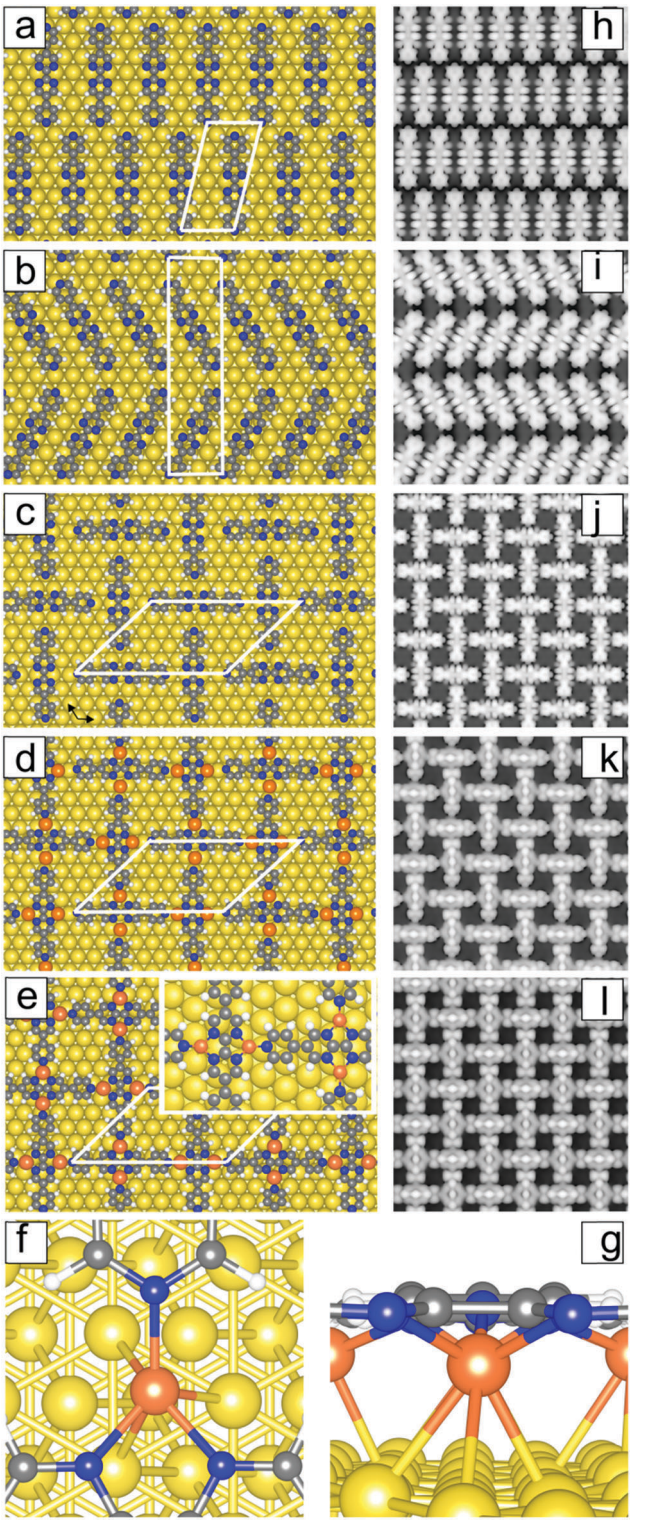

Fig. 4 Optimized surface models for PBP (a–c) and Fe-PBP (d and e) on Au(111). (a) Linear phase (I), (b) zig-zag phase (III), (c) grid phase (II), (d) Fe-PBP, and (e) Fe-PBP on 4% compressed Au(111), and the inset details of the Fe coordination. Fe coordination environment: (f) top view and (g) side view. Colors: yellow, Au atoms; orange, Fe_{ad}; grey, C atoms; blue, N atoms; white, H atoms. Panels (h–l): Simulated STM images of the corresponding surface structures on the left side.

phase formed on the substrate. Gold adatom extraction from the reconstructed surface should be difficult because of the considerable reconstruction energy of the gold surface accompanying the placement of one Au adatom in the molecular lattice. One possibility to incorporate Au adatoms is the detachment from the step edges during sample preparation. In this scenario, the expected low number of gold adatoms kinetically limits the growth of larger islands of phase II and leads to the formation of the other phases at extended deposition times.

The experimental data reveal that incorporation of Fe species results in a complete transformation of phases I and III into phase II (Fig. 3). Therefore, we have modeled the Fe-PBP surface structure by also adding Fe atoms to the $\begin{pmatrix} 9 & 0 \\ -2 & 5 \end{pmatrix}$ surface

lattice. As in the case of Au atom incorporation, we observed that most of Fe atoms accommodate in a Fe–N3 configuration although the Fe species in the [1$\bar{1}$0] direction exhibit Fe–N2 coordination (Fig. 4d). The calculated energetic parameters for this lattice result in $E_{ads} = -12.34$ eV and $\gamma = -73.22$ meV Å^{-2}, *i.e.* the lattice stability markedly increased by the presence of Fe species (Table 1). At this point, it is important to outline that the $(22 \times \sqrt{3})$ Au(111) herringbone reconstruction presents a contraction in the [1$\bar{1}$0] direction. Thus, in Fig. 4e, we have modeled the Fe-PBP overlayer on a surface lattice with the Au neighbor distance contracted by 4%. In this case all Fe species are three-fold coordinated and, accordingly, both $E_{ads} = -13.27$ eV and $\gamma = -86.04$ meV Å^{-2} are slightly higher (Table 1). The higher thermodynamic stability of phase II containing Fe compared to phase II containing Au adatoms presumably leads to the replacement of coordinated Au by Fe.

These results explain the phase selection induced by Fe species as the stability of the PBP lattices increases with the increase in the number of Fe–N interactions. In fact, phases I and III only allow Fe–2N coordination while phase III allows Fe–N3 coordination. Irreversible transformation from Cu–N2 to Cu–N3 coordination has also been reported in 1,3,5-trispyridylbenzene adlayers on Au(111).[24] Therefore, we expect that in the real system, most of the Fe species is Fe–3N coordinated. The higher γ value of the Fe-PBP system compared to simple PBP lattices explains its stability under electrochemical conditions.[26]

In all cases the simulated STM images (Fig. 4h–l) of the different models agree very well with those experimentally observed (Fig. 2).

The calculations also show that the incorporated Fe species are out-of-plane displaced toward the surface by 1.0 Å with respect to PBP, thus explaining why they are not imaged by STM (Fig. 4j), an effect that is accompanied by a low density of states on the Fe species. These are adsorbed on the hollow fcc sites of the Au(111) surface at an average distance of 2.2 Å. The Fe–N distances are 2.1–2.2 Å which are the values similar to those found in the Fe–porphyrin complex adsorbed on Pt(111).[37] However, they are slightly larger than in Fe(II)–N_2 dioxygen complexes (2.07 Å[38]) and Fe–N_4 macrocyclic complexes (1.92–2.1 Å,[37] 1.95 Å[37,39]) as well as in the ligated forms of hemoglobin, cytochrome *c*, oxyhemoglobin, and carbon monoxyhemoglobin where the average Fe–N bond distance is known to be 1.98–1.99 Å.[40,41] From the inset in Fig. 4e, where the Au–Au distances are compressed by 4%, it can be seen that Fe adsorbed at hollow sites presents a six-fold coordinated structure in a pseudo-trigonal prismatic geometry (see also Fig. 4f and g), instead of the usual octahedral geometry present in biological ORR active systems.[42,43] The N_3 coordination also explains the lower electrocatalytic activity for the oxygen reduction reaction of this molecule in relation to the N_4 Fe–phthalocyanine system.[44] Bader analysis shows that the Fe charge density is +1.1/+1.2*e*, indicating that charge transfer is involved in metal–substrate interactions. In fact, the Au surface atoms beneath the Fe species become slightly negative (−0.16/−0.18*e*). The Bader analysis also shows no significant differences in the N atom charges between PBP/Au(111) and Fe-PBP/Au(111) systems. However, the core level shift calculation for the Fe-PBP (Fig. 4d) indicates that on average the BEs of the bipyrimidyl and pyridyl N 1s signals in the Fe-PBP surface structure are shifted to larger values by 0.6 and 0.4 eV, respectively, compared with those in adsorbed PBP (phase II, Fig. 4c). These figures are in excellent agreement with the experimental N 1s shift for the bipyrimidyl (0.8 eV) and pyridyl (0.4 eV) observed in the XPS data (Fig. 3a and b).[40] This fact can be assigned to a chemical shift of the N 1s core level caused by electron charge transfer from the N lone pair of PBP to Fe in a σ-donation. On the other hand, the negligible difference in the N Bader charge can be attributed to a π-back-donation from Fe to N favored by the electron-withdrawing character of the aryl groups of the PBP ligand. However, the charge back-donation does not affect the N 1s core level shift due to its delocalized character against the high localized character of the σ-donation.[45] In our system we estimate the N–Fe bond energy to be about −1.3 eV. Therefore, it can be concluded that the Fe species organize the PBP molecules not only by electron transfer from the N atoms of the PBP molecules to Fe but also by electron transfer from this atom to the Au surface. This could explain the high stability of the Fe-PBP network, which remains intact on the surface even after the transfer from UHV to the electrochemical environment and the realization of electrocatalytic experiments.[26] The next question is to find out how the more stable PBP phases I and III are transformed into the Fe-PBP surface structure. We propose that under the experimental conditions (substrate temperature $T = 413$ K) the highly mobile Fe adatoms arrive on a potentially mobile PBP adlayer, then transfer their charge to the Au substrate (a fast process), and finally the charged adatoms induce the complete rearrangement of the disordered PBP adlayer into the grid structure with N_3 coordination (slow process). We assume that at this substrate temperature, surface diffusion could rearrange phases I and III into phase II since PBP molecules are weakly interacting with the gold substrate.

To address further properties of the coordinated Fe species, we have studied the electronic structure of adsorbed Fe in the PBP adlayer by using a Hubbard-like $+U$ correction[46,47] to describe the density of states. The magnetic properties of coordinated metal centers reveal diverse properties: nitrogen-coordinated Co retains much of its magnetic moment in self-assembled networks,[11] while the high-spin magnetic moment of carboxylate-coordinated Fe centers can be altered through oxygen adsorption.[13] In addition, Kondo resonances have been observed on Fe centers coordinated to pyridyl groups.[48] The distribution of the projected density of states (PDOS) of the Fe-PBP overlayer is depicted in Fig. 5. In this case Fe bonded to three N atoms has been selected to perform the analysis. Fig. 5a shows the change in the localized states of the isolated Fe upon adsorption on Fe-PBP/Au(111). The widespread PDOS of the adsorbed Fe indicates a strong hybridization between Fe d states with the gold substrate d states (Fig. 5b). Also certain interactions between N sp states and Fe d states are observed from our calculations (Fig. 5c). The PDOS plots show that the Fe density of spin-up states (positive states) is greater than spin-down states (negative states). As a consequence, each iron atom in the overlayer has a magnetic moment of 3.0 μ_B approximately

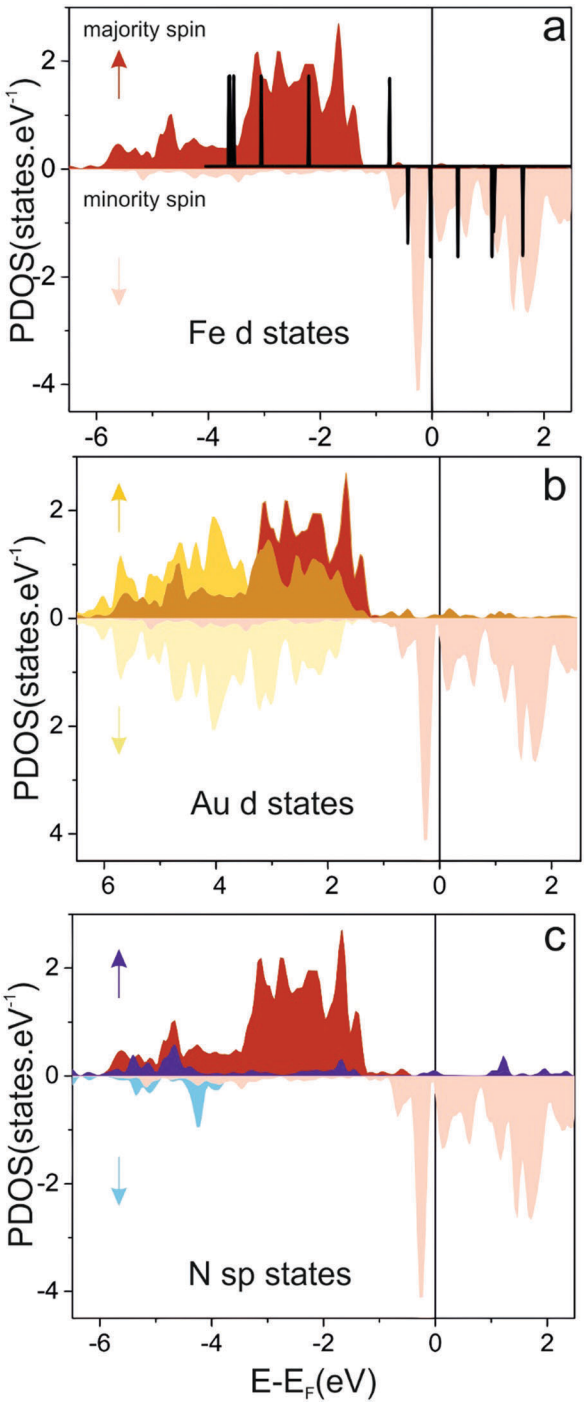

Fig. 5 DFT+U spin-resolved PDOS of Fe-PBP/Au(111). (a) Adsorbed Fe compared with the isolated Fe atom (black lines). (b) Adsorbed Fe and the top Au layer bonded to Fe. (c) Adsorbed Fe and N atoms of the PBP molecule bonded to Fe. Colors: spin up (red) and spin down (light red) of Fe d states; spin up (yellow) and spin down (light yellow) of Au d states; spin up (blue) and spin down (light blue) of N sp states. The black vertical line at E = 0 indicates the position of the Fermi level E_F.

corresponding to the spin state of S = 1. In the same computational framework, a single Fe atom on the Au(111) surface has a magnetic moment of 3.5 μ_B and a charge of +0.49. The missing charge on the Fe atom is distributed in the gold interface. By comparing the results of the single Fe atom with the Fe atoms coordinated in the PBP network, it becomes clear that the effect of the oxidation state is much stronger than of the magnetic moment as the oxidation state doubles whereas the magnetic moment is only slightly decreased.

Conclusions

We have shown that PBP is physisorbed on the herringbone reconstructed Au(111) surface by forming three different well-ordered lattices with similar stabilities. Controlled iron deposition on the organic adlayer results in Fe adatoms, which either transfer their charge to the Au surface or interact to form a few Fe(0) clusters. The presence of the charged Fe species induces structural transformation in the complex PBP adlayer selecting only that PBP lattice which allows the maximum Fe(II)–N coordination sites. In these coordination sites, the Fe species are sixfold-coordinated in a pseudo-trigonal prismatic geometry, with three bonds to the gold substrate and three bonds to nitrogen atoms, instead of the most usual octahedral geometry. The charge transfer from Fe to Au and the Fe–N interaction largely increases the thermodynamic stability of the organic lattice on the Au surface. Our result is a clear demonstration that the structural transformation process induced through Fe incorporation relies on thermodynamic control and kinetic reversibility to allow for error- and self-correction to eliminate other possible structures.

Methods

Network preparation and STM measurements were conducted in a home-built UHV chamber (base pressure $\sim 5 \times 10^{-10}$ mbar).[26] The Au(111) single-crystal substrate (MaTecK) was cleaned by repeated cycles of sputtering with Ar^+ ions and annealing at 825 K. The PBP molecular powder was sublimed from a quartz crucible at 470 K onto the surface held at room temperature using different deposition times to control coverage. To study temperature dependence, after PBP deposition the substrate was post-annealed at 373 K and 423 K. For PBP networks, atomic iron was evaporated onto the surface held at 413 K resulting in nearly-full monolayer network coverage. The STM topographs were acquired at 298 K. The WsXM software was used for image analysis.[49] X-ray photoelectron spectroscopy was performed using a SPECS Phoibos 150 analyzer with a non-monochromatic Mg Kα source ($h\nu$ = 1253.6 eV). Spectral analysis was performed by fitting Voigt functions of a fixed Lorentzian/Gaussian ratio of 80% after subtraction of the background.

DFT calculations for the structural models adsorbed on the Au(111) surface were performed by using the periodic plane-wave set code Vienna Ab initio Simulation Package (VASP 5.2.12) based on density functional theory (DFT).[50,51]

To take into account the van der Waals (vdW) interactions fundamental in this type of study, we have followed the method optB88-vdW,[52] which is a modified version of the vdW-DF functional,[53] by using an empirically optimized optB88-like exchange functional that can accurately describe the intermolecular and the

molecule–substrate interactions.[54,55] The electronic wave functions were expanded in a plane-wave basis set with a cut-off energy of 420 eV. The projector augmented plane wave (PAW) due to the Blöchl method has been used to represent the atomic cores[56] with the PBE potential. Gold surfaces were represented by three atomic layers and a vacuum of ~16 Å separates any two successive slabs. Optimal grids of Monkhorst–Pack[57] k-points $5 \times 2 \times 1$, $5 \times 1 \times 1$ and $1 \times 2 \times 1$ have been used for numerical integration in the reciprocal space of $\begin{pmatrix} 3 & 0 \\ 5 & 7 \end{pmatrix}$, $\begin{pmatrix} 3 & 0 \\ 14 & 7 \end{pmatrix}$ and $\begin{pmatrix} 9 & 0 \\ -2 & 5 \end{pmatrix}$ surface structures respectively. Surface relaxation is allowed in the uppermost Au layer of the slab, and the atomic coordinates of the adsorbed species were allowed to relax without further constraints. The atomic positions were relaxed until the force on the unconstrained atoms was less than 0.03 eV Å^{-1}. The adsorbates are placed just on one side of the slab and all calculations include a dipole correction. The PBP molecule and the Fe atom were optimized in boxes of 30 Å × 29 Å × 28 Å and 16 Å × 16 Å × 16 Å, respectively. All calculations were performed using a spin polarized method. The calculated Au lattice constant is 4.16 Å, which compares reasonably well with the experimental value (4.078 Å).[58]

The Hubbard-like on-site Coulomb and exchange parameters for the Fe 3d orbitals are chosen to be U = 2 eV and J = 1 eV, respectively, and thus $U_{\text{eff}} = U - J$ = 1 eV. These values have been used in previous studies on similar systems.[59,60] Constant current STM images of the optimized lattices were simulated by using the Tersoff–Hamann method in its most basic form, *i.e.* with the STM tip approximated as a point source.[61] The N 1s core-level shift has been determined within the Janak–Slater approach[62] where half a 1s electron has been excited from the core level to the valence region and placed in the lowest unoccupied orbital.

The adsorption energy per unit cell has been defined by

$$E_{\text{ads}} = \left[E_{\text{total}} - E_{\text{Au(111)}} - N_{\text{PBP*}} E_{\text{PBP*}} - N_{\text{Fe}} E_{\text{Fe}}\right] \quad (1)$$

where E_{total}, $E_{\text{Au(111)}}$, E_{PBP}, and E_{Fe} stand for the total energy of the adsorbate–substrate system, the energy of the Au slab, and the energy of one PBP molecule and the energy of the Fe atom, respectively, whereas N_{PBP} and N_{Fe} are the number of PBP molecules and Fe atoms in the surface unit cell. A negative number indicates that adsorption is exothermic with respect to the separate clean surface and the PBP molecule. A description of energy per unit cell, not per molecule, is proposed as the more meaningful approach to describe the energetics of self-assembled structures on surfaces.[63]

The Gibbs free energy of adsorption of the surface structure (γ) was approximated through the total energy from DFT calculations by using eqn [2]:

$$\gamma = \frac{E_{\text{ads}}}{A} \quad (2)$$

where A is the unit cell area. Considering that we are concerned with free energy differences, it is reasonable to assume that the contributions coming from the configurational entropy, the vibrations, and the pressure–volume work termed pV can be neglected.[64,65] In the transformation from one polymorph to the next, translational and rotational entropy changes are zero (no motion in the stabilized self-assembled layer), and also vibrational entropy is assumed to change only insignificantly. Although the contributions from vibrational entropy changes might be sizable,[63] they are about a factor of 10 smaller than changes in enthalpy and are not considered here.

The coverage θ is defined as the number of molecules per the number of underlying gold atoms.

Conflicts of interest

There are no conflicts to declare.

Acknowledgements

The authors acknowledge funding support by the DFG Priority Programs 1928 (COORNETs), TR88 '3Met' and the KNMF facility (KIT, Germany).

References

1 L. Dong, Z. Gao and N. Lin, Self-Assembly of Metal–organic Coordination Structures on Surfaces, *Prog. Surf. Sci.*, 2016, **91**(3), 101–135.
2 R. Gutzler, S. Stepanow, D. Grumelli, M. Lingenfelder and K. Kern, Mimicking Enzymatic Active Sites on Surfaces for Energy Conversion Chemistry, *Acc. Chem. Res.*, 2015, **48**(7), 2132–2139.
3 N. Lin, S. Stepanow, M. Ruben and J. V. Barth, Surface-Confined Supramolecular Coordination Chemistry, *Topics in Current Chemistry*, 2008, vol. 287, pp. 1–44.
4 J. V. Barth, J. Weckesser, N. Lin, A. Dmitriev and K. Kern, Supramolecular Architectures and Nanostructures at Metal Surfaces, *Appl. Phys. A: Mater. Sci. Process.*, 2003, **76**(5), 645–652.
5 J. V. Barth, G. Costantini and K. Kern, Engineering Atomic and Molecular Nanostructures at Surfaces, *Nature*, 2005, **437**(7059), 671–679.
6 Y. Geng, P. Li, J. Li, X. Zhang, Q. Zeng and C. Wang, STM Probing the Supramolecular Coordination Chemistry on Solid Surface: Structure, Dynamic, and Reactivity, *Coord. Chem. Rev.*, 2017, **337**(11), 145–177.
7 T.-C. Tseng, C. Lin, X. Shi, S. L. Tait, X. Liu, U. Starke, N. Lin, R. Zhang, C. Minot and M. A. Van Hove, *et al.*, Two-Dimensional Metal–Organic Coordination Networks of Mn-7,7,8,8-Tetracyanoquinodimethane Assembled on Cu(100): Structural, Electronic, and Magnetic Properties, *Phys. Rev. B: Condens. Matter Mater. Phys.*, 2009, **80**(15), 155458.
8 U. Schlickum, R. Decker, F. Klappenberger, G. Zoppellaro, S. Klyatskaya, M. Ruben, I. Silanes, A. Arnau, K. Kern and H. Brune, *et al.*, Metal–Organic Honeycomb Nanomeshes with Tunable Cavity Size, *Nano Lett.*, 2007, **7**(12), 3813–3817.
9 Q. Sun, L. Cai, H. Ma, C. Yuan and W. Xu, On-Surface Construction of a Metal–organic Sierpiński Triangle, *Chem. Commun.*, 2015, **51**(75), 14164–14166.

10 S. Clair, S. Pons, H. Brune, K. Kern and J. V. Barth, Mesoscopic Metallosupramolecular Texturing by Hierarchic Assembly, *Angew. Chem., Int. Ed.*, 2005, **44**(44), 7294–7297.
11 N. Henningsen, R. Rurali, C. Limbach, R. Drost, J. I. Pascual and K. J. Franke, Site-Dependent Coordination Bonding in Self-Assembled Metal–Organic Networks, *J. Phys. Chem. Lett.*, 2011, **2**(2), 55–61.
12 S. Clair, S. Pons, S. Fabris, S. Baroni, H. Brune, K. Kern and J. V. Barth, Monitoring Two-Dimensional Coordination Reactions: Directed Assembly of Co–Terephthalate Nanosystems on Au(111), *J. Phys. Chem. B*, 2006, **110**(11), 5627–5632.
13 P. Gambardella, S. Stepanow, A. Dmitriev, J. Honolka, F. M. F. de Groot, M. Lingenfelder, S. S. Gupta, D. D. Sarma, P. Bencok and S. Stanescu, *et al.*, Supramolecular Control of the Magnetic Anisotropy in Two-Dimensional High-Spin Fe Arrays at a Metal Interface, *Nat. Mater.*, 2009, **8**(3), 189–193.
14 D. Skomski, C. D. Tempas, K. A. Smith and S. L. Tait, Redox-Active On-Surface Assembly of Metal–Organic Chains with Single-Site Pt(II), *J. Am. Chem. Soc.*, 2014, **136**(28), 9862–9865.
15 D. Skomski, C. D. Tempas, B. J. Cook, A. V. Polezhaev, K. A. Smith, K. G. Caulton and S. L. Tait, Two- and Three-Electron Oxidation of Single-Site Vanadium Centers at Surfaces by Ligand Design, *J. Am. Chem. Soc.*, 2015, **137**(24), 7898–7902.
16 Y. Li, J. Xiao, T. E. Shubina, M. Chen, Z. Shi, M. Schmid, H. P. Steinrück, J. M. Gottfried and N. Lin, Coordination and Metalation Bifunctionality of Cu with 5,10,15,20-tetra(4-Pyridyl)porphyrin: Toward a Mixed-Valence Two-Dimensional Coordination Network, *J. Am. Chem. Soc.*, 2012, **134**(14), 6401–6408.
17 J. Mielke, F. Hanke, M. V. Peters, S. Hecht, M. Persson and L. Grill, Adatoms underneath Single Porphyrin Molecules on Au(111), *J. Am. Chem. Soc.*, 2014, **137**(111), 1844–1849.
18 M. S. Dyer, A. Robin, S. Haq, R. Raval, M. Persson and J. Klimeŝ, Understanding the Interaction of the Porphyrin Macrocycle to Reactive Metal Substrates: Structure, Bonding, and Adatom Capture, *ACS Nano*, 2011, **5**(3), 1831–1838.
19 W. Zhou, *Three-Dimensional Nanoarchitectures*, ed. W. Zhou and Z. L. Wang, Springer, New York, NY, 2011.
20 F. Buchner, K. Flechtner, Y. Bai, E. Zillner, I. Kellner, H.-P. Steinrück, H. Marbach and J. M. Gottfried, Coordination of Iron Atoms by Tetraphenylporphyrin Monolayers and Multilayers on Ag(111) and Formation of Iron-Tetraphenylporphyrin, *J. Phys. Chem. C*, 2008, **112**(39), 15458–15465.
21 K. Flechtner, A. Kretschmann, H.-P. Steinrück and J. M. Gottfried, NO-Induced Reversible Switching of the Electronic Interaction between a Porphyrin-Coordinated Cobalt Ion and a Silver Surface, *J. Am. Chem. Soc.*, 2007, **129**(40), 12110–12111.
22 Y. Bai, M. Sekita, M. Schmid, T. Bischof, H.-P. Steinrück and J. M. Gottfried, Interfacial Coordination Interactions Studied on Cobalt Octaethylporphyrin and Cobalt Tetraphenylporphyrin Monolayers on Au(111), *Phys. Chem. Chem. Phys.*, 2010, **12**(17), 4336.
23 M. Chen, X. Feng, L. Zhang, H. Ju, Q. Xu, J. Zhu, J. M. Gottfried, K. Ibrahim, H. Qian and J. Wang, Direct Synthesis of Nickel(II) Tetraphenylporphyrin and Its Interaction with a Au(111) Surface: A Comprehensive Study, *J. Phys. Chem. C*, 2010, **114**(21), 9908–9916.
24 J. Liu, T. Lin, Z. Shi, F. Xia, L. Dong, P. N. Liu and N. Lin, Structural Transformation of Two-Dimensional Metal-Organic Coordination Networks Driven by Intrinsic in-Plane Compression, *J. Am. Chem. Soc.*, 2011, **133**(46), 18760–18766.
25 S. L. Tait, A. Langner, N. Lin, R. Chandrasekar, O. Fuhr, M. Ruben and K. Kern, Assembling Isostructural Metal-Organic Coordination Architectures on Cu(100), Ag(100) and Ag(111) Substrates, *ChemPhysChem*, 2008, **9**(17), 2495–2499.
26 D. Grumelli, B. Wurster, S. Stepanow and K. Kern, Bio-Inspired Nanocatalysts for the Oxygen Reduction Reaction, *Nat. Commun.*, 2013, **4**, 2904.
27 G. Wang, A. Rühling, S. Amirjalayer, M. Knor, J. B. Ernst, C. Richter, H.-J. H. Gao, A. Timmer, H.-J. H. Gao and N. L. Doltsinis, *et al.*, Ballbot-Type Motion of N-Heterocyclic Carbenes on Gold Surfaces, *Nat. Chem.*, 2016, **9**(2), 152–156.
28 H. Zhang, J.-H. H. Franke, D. Zhong, Y. Li, A. Timmer, O. D. Arado, H. Mönig, H. Wang, L. Chi and Z. Wang, *et al.*, Surface Supported Gold-Organic Hybrids: On-Surface Synthesis and Surface Directed Orientation, *Small*, 2014, **10**(7), 1361–1368.
29 H. Zhang and L. Chi, Gold–Organic Hybrids: On-Surface Synthesis and Perspectives, *Adv. Mater.*, 2016, **28**(47), 10492–10498.
30 A. Langner, S. L. Tait, N. Lin, R. Chandrasekar, V. Meded, K. Fink, M. Ruben and K. Kern, Selective Coordination Bonding in Metallo-Supramolecular Systems on Surfaces, *Angew. Chem., Int. Ed.*, 2012, **51**(18), 4327–4331.
31 T. Boland and B. D. Ratner, Two-Dimensional Assembly of Purines and Pyrimidines on Au(111), *Langmuir*, 1994, **10**(10), 3845–3852.
32 S. Herrera, F. Tasca, F. J. Williams, E. J. Calvo, P. Carro and R. C. Salvarezza, Surface Structure of 4-Mercaptopyridine on Au(111): A New Dense Phase, *Langmuir*, 2017, **33**(38), 9565–9572.
33 E. Mateo-Martí, C. Briones, C. M. Pradier and J. A. Martín-Gago, A DNA Biosensor Based on Peptide Nucleic Acids on Gold Surfaces, *Biosens. Bioelectron.*, 2007, **22**(9–10), 1926–1932.
34 K. Artyushkova, B. Kiefer, B. Halevi, A. Knop-Gericke, R. Schlogl and P. Atanassov, Density Functional Theory Calculations of XPS Binding Energy Shift for Nitrogen-Containing Graphene-like Structures, *Chem. Commun.*, 2013, **49**(25), 2539.
35 M. Schmid, J. Zirzlmeier, H.-P. Steinrück and J. M. Gottfried, Interfacial Interactions of Iron(II) Tetrapyrrole Complexes on Au(111), *J. Phys. Chem. C*, 2011, **115**(34), 17028–17035.
36 D. K. Lavallee, J. Brace and N. Winograd, X-Ray Photoelectron Spectra of N-Methyltetraphenylporphyrins: Evidence for a Correlation of Binding Energies with Metal-Nitrogen Bond Distances, *Inorg. Chem.*, 1979, **18**(7), 1776–1780.
37 D. P. Miller, J. Hooper, S. Simpson, P. S. Costa, N. Tymińska, S. M. McDonnell, J. A. Bennett, A. Enders and E. Zurek, Electronic Structure of Iron Porphyrin Adsorbed to the Pt(111) Surface, *J. Phys. Chem. C*, 2016, **120**(51), 29173–29181.
38 J. P. Collman, R. R. Gagne, C. A. Reed, W. T. Robinson and G. A. Rodley, Structure of an Iron(II) Dioxygen Complex;

A Model for Oxygen Carrying Hemeproteins, *Proc. Natl. Acad. Sci. U. S. A.*, 1974, **71**(4), 1326–1329.

39 S. J. Brown, M. M. Olmstead and P. K. Mascharak, Iron(II) and iron(III) Complexes of *N*-(2-(4-Imidazolyl)ethyl)pyrimidine-4-Carboxamide, a Ligand Resembling Part of the Metal-Binding Domain of Bleomycin, *Inorg. Chem.*, 1990, **29**(17), 3229–3234.

40 R. A. Lewis, K. C. MacLeod, B. Q. Mercado and P. L. Holland, Geometric and Redox Flexibility of Pyridine as a Redox-Active Ligand That Can Reversibly Accept One or Two Electrons, *Chem. Commun.*, 2014, **50**(76), 11114.

41 P. Eisenberger, R. G. Shulman, G. S. Brown and S. Ogawa, Structure-Function Relations in Hemoglobin as Determined by X-Ray Absorption Spectroscopy (Cooperative Oxygenation/heme-Heme Interaction), *Biophysics*, 1976, **73**(2), 491–495.

42 J. Echeverría, E. Cremades, A. J. Amoroso and S. Alvarez, Jahn–Teller Distortions of Six-Coordinate CuII Compounds: Cis or Trans?, *Chem. Commun.*, 2009, (28), 4242.

43 L. J. Alcock, G. Cavigliasso, A. C. Willis, R. Stranger and S. F. Ralph, Trigonal Prismatic Metal Complexes: A Not so Rare Coordination Geometry?, *Dalton Trans.*, 2016, **45**(22), 9036–9040.

44 B. Wurster, D. Grumelli, D. Hötger, R. Gutzler and K. Kern, Driving the Oxygen Evolution Reaction by Nonlinear Cooperativity in Bimetallic Coordination Catalysts, *J. Am. Chem. Soc.*, 2016, **138**(11), 3623–3626.

45 R. H. Crabtree, *The Organometallic Chemistry of the Transition Metals*, Wiley Interscience, 4th edn, 2005.

46 S. L. Dudarev, G. A. Botton, S. Y. Savrasov, C. J. Humphreys and a. P. Sutton, Electron-Energy-Loss Spectra and the Structural Stability of Nickel Oxide: An LSDA+*U* Study, *Phys. Rev. B: Condens. Matter Mater. Phys.*, 1998, **57**(3), 1505–1509.

47 A. I. Liechtenstein, V. I. Anisimov and J. Zaanen, Density-Functional Theory and Strong Interactions: Orbital Ordering in Mott-Hubbard Insulators, *Phys. Rev. B: Condens. Matter Mater. Phys.*, 1995, **52**(8), R5467–R5470.

48 T. Lin, G. Kuang, W. Wang and N. Lin, Two-Dimensional Lattice of Out-of-Plane Dinuclear Iron Centers Exhibiting Kondo Resonance, *ACS Nano*, 2014, **8**(8), 8310–8316.

49 I. Horcas, R. Fernández, J. M. Gómez-Rodríguez, J. Colchero, J. Gómez-Herrero and A. M. Baro, WSXM: A Software for Scanning Probe Microscopy and a Tool for Nanotechnology, *Rev. Sci. Instrum.*, 2007, **78**(1), 13705.

50 G. Kresse and J. Furthmüller, Efficiency of Ab-Initio Total Energy Calculations for Metals and Semiconductors Using a Plane-Wave Basis Set, *Comput. Mater. Sci.*, 1996, **6**(1), 15–50.

51 G. Kresse and J. Hafner, Ab Initio Molecular Dynamics for Open-Shell Transition Metals, *Phys. Rev. B: Condens. Matter Mater. Phys.*, 1993, **48**(17), 13115–13118.

52 J. Klimeš, D. D. R. Bowler, A. Michaelides, J. Klimes, D. D. R. Bowler, A. Michaelides, J. Klimeš, D. D. R. Bowler and A. Michaelides, Chemical Accuracy for the van der Waals Density Functional, *J. Phys.: Condens. Matter*, 2010, **22**(2), 22201.

53 M. Dion, H. Rydberg, E. Schröder, D. C. Langreth and B. I. Lundqvist, van der Waals Density Functional for General Geometries, *Phys. Rev. Lett.*, 2004, **92**(24), 246401.

54 W. Lew, M. C. Crowe, C. T. Campbell, J. Carrasco and A. Michaelides, The Energy of Hydroxyl Coadsorbed with Water on Pt(111), *J. Phys. Chem. C*, 2011, **115**(46), 23008–23012.

55 M. A. Floridia Addato, A. A. Rubert, G. A. Benítez, M. H. Fonticelli, J. Carrasco, P. Carro and R. C. Salvarezza, Alkanethiol Adsorption on Platinum: Chain Length Effects on the Quality of Self-Assembled Monolayers, *J. Phys. Chem. C*, 2011, **115**(36), 17788–17798.

56 P. E. Blöchl, Projector Augmented-Wave Method, *Phys. Rev. B: Condens. Matter Mater. Phys.*, 1994, **50**(24), 17953–17979.

57 H. J. Monkhorst and J. D. Pack, Special Points for Brillouin-Zone Integrations, *Phys. Rev. B: Solid State*, 1976, **13**(12), 5188–5192.

58 W. B. Pearson, *A Handbook of Lattice Spacing and Structure of Metals*, Pergamon Press, Inc., New York, 4th edn, 1958.

59 Y. Wang, X. Zheng and J. Yang, Environment-Modulated Kondo Phenomena in FePc/Au(111) Adsorption Systems, *Phys. Rev. B*, 2016, **93**(12), 125114.

60 E. Minamitani, N. Tsukahara, D. Matsunaka, Y. Kim, N. Takagi and M. Kawai, Symmetry-Driven Novel Kondo Effect in a Molecule, *Phys. Rev. Lett.*, 2012, **109**(8), 86602.

61 J. Tersoff and D. R. Hamann, Theory of the Scanning Tunneling Microscope, *Phys. Rev. B: Condens. Matter Mater. Phys.*, 1985, **31**(2), 805–813.

62 J. F. Proof That Janak, $\partial E/\partial n_i = \varepsilon_i$ in Density-Functional Theory, *Phys. Rev. B: Condens. Matter Mater. Phys.*, 1978, **18**(12), 7165–7168.

63 S. Conti and M. Cecchini, Predicting Molecular Self-Assembly at Surfaces: A Statistical Thermodynamics and Modeling Approach, *Phys. Chem. Chem. Phys.*, 2016, **18**(46), 31480–31493.

64 K. Reuter and M. Scheffler, Composition, Structure, and Stability of RuO2(110) as a Function of Oxygen Pressu, *Phys. Rev. B: Condens. Matter Mater. Phys.*, 2001, **65**(3), 35406.

65 D. Torres, P. Carro, R. C. Salvarezza and F. Illas, Evidence for the Formation of Different Energetically Similar Atomic Structures in Ag(111)-(7 × 7)-R19.1-CH3S, *Phys. Rev. Lett.*, 2006, **97**(22), 226103.